RESEARCH ARTICLE

Check for updates

A highly durable zinc-air battery from a directly integrated Fe$_x$NC@NiFe(OH)$_x$ bifunctional catalyst†

Hao Luo, [a] Yang Li, [b] Wenchao Wang, [a] Tao Zhou[a] and Zhengxiao Guo *[a]

Rechargeable zinc-air batteries (ZABs) hold great promise for energy storage and conversion due to their high theoretical energy density, cost-effectiveness, and inherent safety. However, progress is constrained by sluggish oxygen electrocatalysis and instability at the air cathode. To address such issues, we resort to a directly integrated pseudo-3D composite electrocatalyst based on carbon cloth, on which Fe/Fe$_3$C- and N- co-doped carbon nanotubes are directly induced and then used to further intercalate NiFe hydroxide clusters, Fe$_x$NC@NiFe(OH)$_x$. This hierarchical electrocatalyst shows enhanced oxygen electrocatalysis (ΔE is 636 mV), rendering high efficiency and durability of ZABs. Such improvement can be attributed to the rationally integrated pseudo-3D structure with high conductivity, high density of active sites, interconnected porosity, and well-bonded components for accelerating electron transfer and ion diffusion while ensuring structural integrity. Moreover, the hierarchical structure increases the electrochemical surface area with superior surface hydrophilicity. As a result, the composite electrocatalyst shows great potential as a binder-free air electrode, as demonstrated in a rechargeable ZAB of a high power density of 85.1 mW cm^{-2} and a long period of operation beyond 2000 cycles (350 h) without notable degradation, outperforming noble metal electrodes.

Introduction

Expeditious exploitation of clean energy storage and conversion technologies is imperative to mitigate climate change, enhance energy efficiency, and integrate renewable energy resources. Rechargeable zinc-air batteries (ZABs) hold great promise due to their high theoretical energy density, cost-effectiveness, and inherent safety.[1–7] Nevertheless, scale-up applications are still hindered by unsatisfactory performance, particularly due to the unstable and sluggish oxygen electrocatalysis at the air cathode.[8–12] The oxygen evolution and reduction reactions (OER/ORR) proceed by a multi-step proton-coupled electron transfer process, normally necessitating noble metals to expedite the reaction kinetics, such as the benchmarking Pt-based (Pt/C) for ORR and the Ir/Ru-based for OER.[13–16] However, the exiguous nature and high cost of noble metals also challenge the wide applications of ZABs. Therefore, extensive efforts have been devoted to synthesizing noble metal-free electrodes for highly efficient oxygen electrocatalysis.[17–25] Cost-

effective bifunctional catalytic electrocatalysts that can accelerate both the ORR and OER have sprung up for high-performance ZABs.[26–31]

Transition metal (TM) compounds embedded in nitrogen (N)-doped carbon electrocatalysts have been screened for efficient oxygen reduction.[32–36] Previous experiments and simulations of such composites have demonstrated that the enhancement of Fe/Fe$_3$C nanoparticles and Fe–N$_x$ coordinated moieties for ORR arises from the interplay between the metal sites and the N-doped carbon lattices, where the well-tuned electronic structure leads to optimized adsorption affinity towards successively generated intermediates.[37–41] Although Fe/Fe$_3$C@NC is effective in catalysing ORR, their catalytic performance for OER cannot compete with the state-of-the-art OER catalytic electrodes, nickel-iron hydroxide (NiFe (OH)$_x$).[42,43] NiFe(OH)$_x$ is characterized by a layered structure with alternating metal cations and intercalated solvent molecules. Despite high intrinsic activity for OER, it suffers from poor electrical conductivity and insufficiently exposed active sites.[44–46]

From the above, it is clear that it is challenging for a single component electrode to satisfy the need for oxygen electrocatalysis because of the mechanistic incompatibility of facilitating OER and ORR into reversible reactions.[47–50] For instance, in an alkaline solution, despite sharing the same reaction intermediates (O*, OH*, OOH*), the additional initial step of the adsorp-

[a]Department of Chemistry, The University of Hong Kong, Hong Kong SAR, China. E-mail: zxguo@hku.hk
[b]Department of Mechanical and Aerospace Engineering, The Hong Kong University of Science and Technology, Clear Water Bay, Hong Kong SAR, China
†Electronic supplementary information (ESI) available. See DOI: https://doi.org/10.1039/d2qi02564g

1758 | *Inorg. Chem. Front.*, 2023, **10**, 1758–1768

This journal is © the Partner Organisations 2023

tion of OH^- ions for OER or the activation of O_2 molecules for ORR is crucial for accelerating the whole catalytic process, which challenges the single component to realize bifunctional specificity.[51–54] In comparison, two-component heterojunction catalysts can integrate the merits of both and realize high catalytic activities for both OER and ORR.[55] For example, atomic Co–N–C and Co_3O_4 nanoparticles were selected as ORR and OER electrocatalysts, respectively, yielding a robust bifunctional electrode for rechargeable ZABs,[56] with a relatively long lifespan of 2250 cycles at 5 mA cm^{-2} and 365 cycles at 10 mA cm^{-2}. Gao *et al.* proposed a novel composite electrocatalyst constructed by bimetallic phosphide CoFeP nanoparticles embedded in N,P co-doped carbon matrix, where the former provides ample OER active sites and the latter promises high ORR activity.[57] The corresponding ZAB attains a large power density of 143.5 mW cm^{-2} and long operation life of 1200 cycles (200 h). Recently, Lin and co-workers innovatively integrated wrinkled MoS_2 nanospheres with a layer of single Fe–N–C shell as OER and ORR active components, respectively.[58] The Fe–N–C shell protects the MoS_2 core from oxidation, enhancing the cycling stability at a power density of 78 mW cm^{-2} for the corresponding wearable ZABs. However, most studies focus more on synthesizing oxygen catalysts, ignoring the drawback of these planar electrodes where additional binder buries active sites, and the electron transfer/ion diffusion is blocked. Moreover, the porous electrodes are crucial components of high-performance electrochemical batteries, which enlarge the electrodes/electrolyte interface to three-dimension. While the rate depends on both the specific surface area of oxygen catalysts and the efficacy of electron transfer and ion diffusion. Additionally, oxygen electrocatalysis occurs on the air–liquid–solid triple phase junction, requiring high mobility of the reactive species, namely, O_2 in air, ions in liquid (electrolyte) and electrons in solid (electrode), readily accessible active sites, and sustained structural durability.[59–61] There is a lack of consideration of such heuristic design principles for the fabrication of bifunctional composite electrodes regarding the selection of active components and electrode structures.[62–65]

Here, a long-lifespan rechargeable zinc-air battery is achieved by constructing a pseudo-3D composite electrocatalyst that combines "directly-grown-on-support" Fe/Fe$_3$C- and N-co-doped carbon nanotubes with NiFe(OH)$_x$ (Fe$_x$NC@NiFe(OH)$_x$). In this way, OER active sites provided by NiFe(OH)$_x$ clusters can be connected to the electron transport pathway due to the high conductive Fe$_x$NC network. Correspondingly, the hydrophilicity of NiFe(OH)$_x$ also promises intimate contact between Fe$_x$NC with oxygen reactant. Such a unique configuration promises effective electron/ion transfer, abundant active sites, interfacial hydrophilicity for oxygen diffusion, and structural integrity. Consequently, the composite electrode shows remarkable ORR and OER performance with a voltage gap of 636 mV, far better than their respective individual components. The ZAB with the binder-free air composite cathode (Fe$_x$NC@NiFe(OH)$_x$) shows higher power density and longer operation life than the noble electrode (Pt/C//RuO$_2$).

Experimental section

Chemicals

Potassium ferricyanide, ferric chloride, dicyandiamide, concentrated HNO_3, concentrated HCl, iron(II) sulfate heptahydrate, nickel(II) nitrate hexahydrate, Pt/C (20%), and RuO_2 were all used without further purification.

Material synthesis

Fabrication of Fe$_x$NC. Typically, commercial carbon cloth was treated in concentrated HNO_3 under ultrasonication for 1 h and rinsed with deionized water. 0.496 g $K_3Fe(CN)_6$ was dissolved in 15 ml deionized water and then poured into $FeCl_3$ solution (25 ml, 0.41 g), followed by stirring at room temperature for 5 min to form a homogeneous solution. Then, a piece of pre-treated carbon cloth (2 cm × 3 cm) was added to the solution and heated at 60 °C for 6 h. After cooling to room temperature, the carbon cloth was taken out and washed thoroughly with deionized water and dried in the vacuum oven at 80 °C overnight.[66] The above carbon cloth and 1.0 g dicyandiamide were put into the same porcelain boat with a cover. Then, the sample was calcined at 400 °C for 2 h in N_2 atmosphere and then annealed at 850 °C for another 2 h. The heating rate was kept at 3 °C min^{-1}. To remove unstable iron species, the annealed electrode was immersed in 2 M HCl for 12 h at 65 °C. Afterward, the electrode was washed with water and dried at 80 °C for 6 h. The loading amount of active material on carbon cloth was ~0.8 mg cm^{-2}.

Fabrication of Fe$_x$NC@NiFe(OH)$_x$. Electrodeposition of nickel–iron hydroxide was carried out in a standard three-electrode electrochemical cell, employing the prepared Fe$_x$NC as the working electrode, carbon rod as the counter electrode, and saturated calomel electrode (SCE) as the reference electrode.[53] The aqueous electrochemical bath consists of 0.436 g of Ni(NO$_3$)$_2$·6H$_2$O and 0.417 g of FeSO$_4$·7H$_2$O. After maintaining a fixed electrodeposition current density of 20 mA cm^{-2} for 5 min, the Fe$_x$NC@NiFe(OH)$_x$ electrode was obtained with a loading amount of ~2.8 mg cm^{-2} NiFe(OH)$_x$. Different deposition times of 0.3 min and 10 min were also investigated to optimize the performance.

Fabrication of Pt and RuO$_2$ on carbon cloth. A sample of 4 mg Pt/C (20%) was dispersed in a solvent mixture with 500 μl ethanol, 470 μl water, and 30 μl Nafion (0.5 wt%), followed by mixing with ultrasonication for 3 h to obtain a homogeneous ink. 200 μl of the catalyst ink was pipetted onto a piece of carbon cloth as the electrode (1 cm × 1 cm). The loading mass of 20% Pt/C was ~0.8 mg cm^{-2}. Commercial RuO$_2$ was also used for comparison of OER, where 10 mg RuO$_2$ was dispersed in the above solution and sonicated for 3 h. The loading mass of RuO$_2$ suspensions on carbon cloth was ~2.8 mg cm^{-2}.

Material characterization

The morphology and microstructure of the samples were characterized by scanning electron microscopy (SEM MAIA3) and transmission electron microscopy (JEM-2010, JEOL).

This journal is © the Partner Organisations 2023

Inorg. Chem. Front., 2023, **10**, 1758–1768 | **1759**

Powder X-ray diffraction (Bruker D8, PXRD) was used to identify the phase structures of the electrode components. The surface chemistry of the electrode was analyzed by X-ray photoelectron spectroscopy (XPS, Kratos Axis Ultra). The contact angle measurement instrument was used to examine the hydrophilicity of the electrode with the electrolyte (Dataphysics, OCA 20). Nitrogen adsorption–desorption was performed on the adsorption apparatus (Micromeritics, ASAP2460). As-prepared electrodes were cut into small fragments using scissors for tests. The surface area and pore size distribution were fitted by the Brunauer–Emmett–Teller (BET) method and the Barrett–Joyner–Halenda (BJH) method, respectively.

Electrochemical test

Electrochemical tests were carried out on an electrochemical station (CHI 760E) using a standard three-electrode system. A saturated calomel electrode (SCE) and carbon rod worked as the reference electrode and counter electrode, respectively. The electrolyte was 0.1 M KOH for OER and ORR. Catalysts supported on carbon cloth were directly used as the working electrode. All potentials in this work were calibrated to the reversible hydrogen electrode (RHE) by the following equation:

$$E_{RHE} = E_{SCE} + 0.241 + 0.059 \ pH$$

OER and ORR performances were accessed *via* linear sweep voltammetry (LSV) with 95%-*iR* compensation. OER was evaluated with a scan rate of 2 mV s^{-1} from 0.2 to 1.0 V *vs.* SCE, and ORR was measured at a scan rate of 10 mV s^{-1} from 0 to -0.6 V *vs.* SCE. The electrochemical active surface area (ECSA) of the electrodes was estimated by comparing double-layer capacitances (C_{dl}), which were obtained by scanning cyclic voltammetry (CV) at different rates of 10, 30, 50, 70, and 90 mV s^{-1} in the non-faradaic potential region (0–0.1 V *vs.* SCE). From the linear fitting of the line of the current density difference at 0.050 V *vs.* SCE against the above scan rates, the slope is C_{dl}. ZAB test was performed under an atmospheric environment using a homemade cell. A polished zinc plate (500 μm in thickness) was used as a cathode. The aqueous solution containing 6 M KOH and 0.2 M zinc acetate was used as the electrolyte. Fe$_x$NC@NiFe(OH)$_x$ supported on carbon cloth and a gas diffusion layer were combined as the air cathode. The effective area of the air cathode was 1 × 1 cm^2. Galvanostatic discharge–charge cycling tests were evaluated using a LAND CT3001A battery test system at 10 mA cm^{-2} with 5 min discharge and 5 min charge per cycle. For comparison, 20% Pt (0.8 mg cm^{-2}) and RuO$_2$ (2.8 mg cm^{-2}) were also loaded on the carbon cloth as the air cathode.

Results and discussion

As depicted in Fig. 1a, the rational fabrication strategy of the bifunctional Fe$_x$NC@NiFe(OH)$_x$ electrode involves three steps: (1) the immobilization of FeFe(CN)$_6$ nano-seeds on carbon cloth by a wet-chemistry method; (2) carbonization facilitating the growth of N-doped carbon nanotubes (CNTs) catalyzed by

in situ evolved Fe/Fe$_3$C; and (3) electrodeposition of NiFe(OH)$_x$ clusters over the CNTs. Details of the synthesis process are provided in the experimental section. For the first step, as shown in the scanning electron microscopy image (SEM, Fig. S1a and b†), uniform FeFe(CN)$_6$ nano-seeds are tightly anchored on the carbon cloth (CC) by facile solution precipitation. Subsequently, under high-temperature pyrolysis at 850 °C, the FeFe(CN)$_6$ precursors are decomposed, forming entangled CNTs on the CC (Fig. 1b and c). Transmission electron microscopy (TEM) images show that dark particles are enveloped in the middle or tips of the CNTs (Fig. 1d). The high-resolution TEM displays well-defined lattice fringes, which are consistent with the (211) and (110) crystalline planes of Fe/Fe$_3$C (Fig. S2a†). The average size of metal nanoparticles is around 30–40 nm (Fig. S2b†). The X-ray diffraction (XRD) patterns confirm the co-existence of Fe and Fe$_3$C (green curve), where the diffraction peaks are attributed to crystalline planes (102) of Fe$_3$C at 43.7° (JCPDS No. 35–0772) and (110) and (211) planes at 44.7° and 65.2° of metallic Fe (JCPDS No. 06–0696), respectively (Fig. 1e).

Raman spectra further probe the crystallinity of the carbons. The D band (1357 cm^{-1}) signal reflects the vibrational environment of defective/disordered carbon, and the G band (1560 cm^{-1}) shows the graphitic/crystalline carbon structure.[67,68] As illustrated in Fig. S2c,† the intensity ratio of D to G of Fe$_x$NC is 0.58, indicating a high degree of crystallinity of the carbon tubes. The highly graphitized carbon endows 3D conductive and porous networks for electron transfer and ion transport. Energy-dispersive X-ray spectroscopy (EDS) elemental mapping images reveal the uniform distribution of Fe, N, and C in the nanotube matrix (Fig. S2d†), and their respective proportions have also been measured (Table S1†). From the elemental mapping images, apart from the signal of relatively large aggregates of Fe/Fe$_3$C, Fe element is also enriched on the carbon wall.

The facile electrodeposition technique is used to immobilize NiFe(OH)$_x$ onto the as-prepared nanotubes. As revealed by the SEM images in Fig. 1f and g, platelet-like NiFe(OH)$_x$ clusters are uniformly decorated on the surface of CNTs after rapid electrodeposition for only 5 min, denoted as Fe$_x$NC@NiFe(OH)$_x$. The hierarchical nanotubes provide a high surface area for the growth of the nanosheets and avert undesirable aggregation, as compared with electrodeposition of NiFe(OH)$_x$ on pristine CC surface (Fig. S3a and b†). The schematic diagram shown in Fig. 1h manifests the merits of the integrated 3D electrode for oxygen electrocatalysis with high electron transfer, ion transport, and dual active components. XRD patterns further verify the amorphous nature of the deposited NiFe(OH)$_x$ (Fig. 1e and Fig. S3c, d†). The amorphous NiFe(OH)$_x$ exhibits better catalytic activity than the crystalline counterpart due to more unsaturated active sites.[69–71] Fig. 1i shows the TEM and EDS mapping images of Fe$_x$NC@NiFe(OH)$_x$, revealing that nanoplates are tightly grown on the nanotubes with uniform dispersions of Ni, Fe, and O elements.

The electrodeposition time largely determines the amount of NiFe(OH)$_x$, which may, in turn, affect the catalytic activity
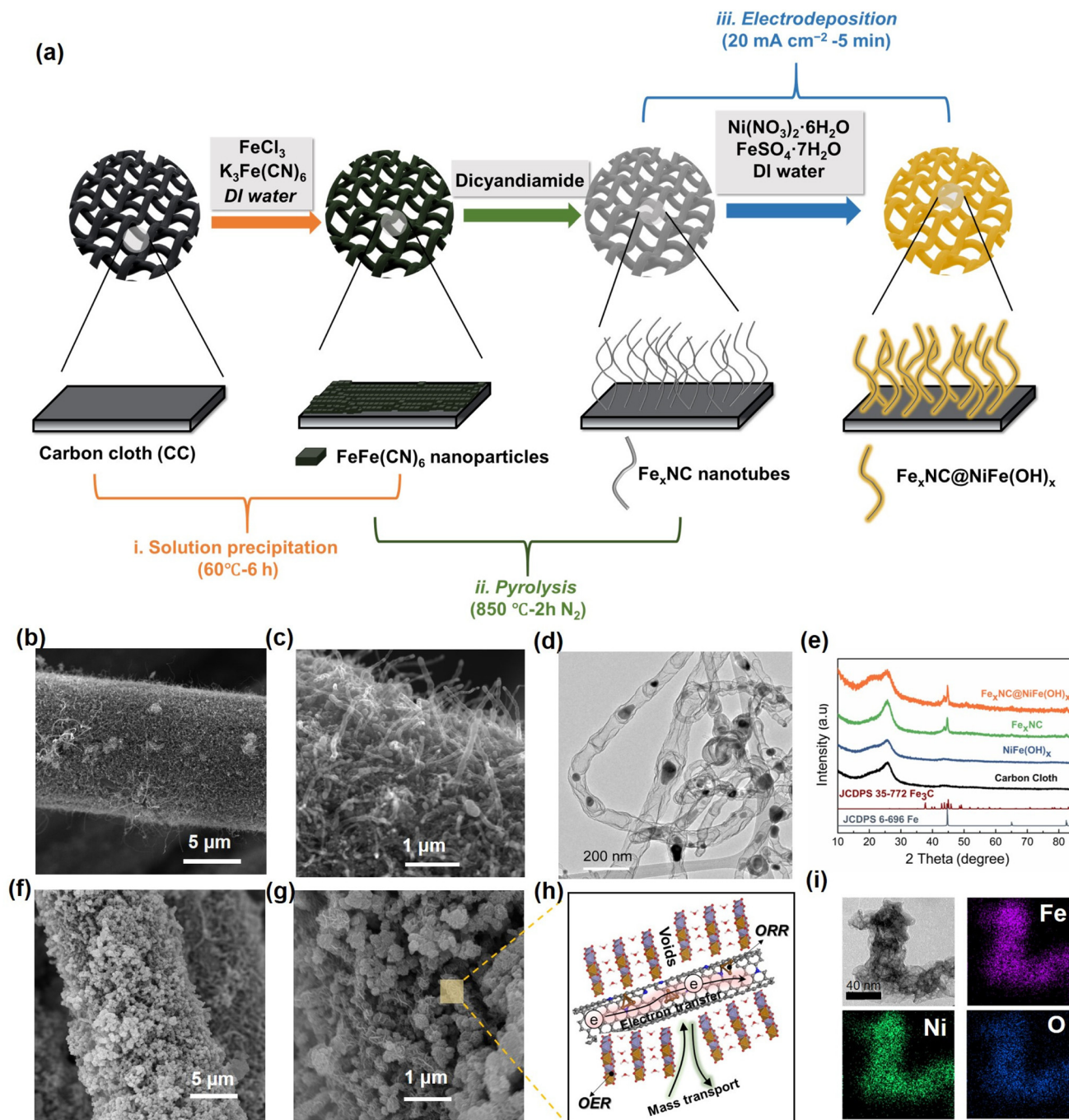
1760 | *Inorg. Chem. Front.*, 2023, **10**, 1758–1768

This journal is © the Partner Organisations 2023

Fig. 1 (a) Schematic illustration of the synthesis route for $Fe_xNC@NiFe(OH)_x$. (b–d) SEM and TEM images of Fe_xNC. (e) XRD patterns of as-prepared electrodes. (f and g) SEM images of $Fe_xNC@NiFe(OH)_x$ and (h) the corresponding schematic diagram. (i) TEM image of $Fe_xNC@NiFe(OH)_x$ and EDS elemental mapping images.

and mass transfer properties. For comparison, shorter (0.3 min) and longer (10 min) periods of deposition time were also accessed, denoted as $Fe_xNC@NiFe(OH)_x$-0.3 and $Fe_xNC@NiFe(OH)_x$-10, respectively. Their morphologies are shown in Fig. S4,† revealing that the shorter time leads to loosely deposited layers on the nanotubes, whereas the longer deposition time causes excessive aggregation of deposits over the electrode surface.

X-ray photoelectron spectroscopy (XPS) is conducted to determine the surface composition and valence states. In the survey spectrum, $Fe_xNC@NiFe(OH)_x$ shows a similar pattern to pristine $NiFe(OH)_x$ due to the detection limit (~10 nm) of the surface detection technique (Fig. S5†). For Fe_xNC, the high-resolution N 1s spectrum shows five peaks: oxidized-N (402.8 eV), graphitic-N (401.3 eV), pyrrolic-N (400.3 eV), Fe_x–N (399.4 eV), and pyridinic-N (398.4 eV) (Fig. 2a). The proportion of

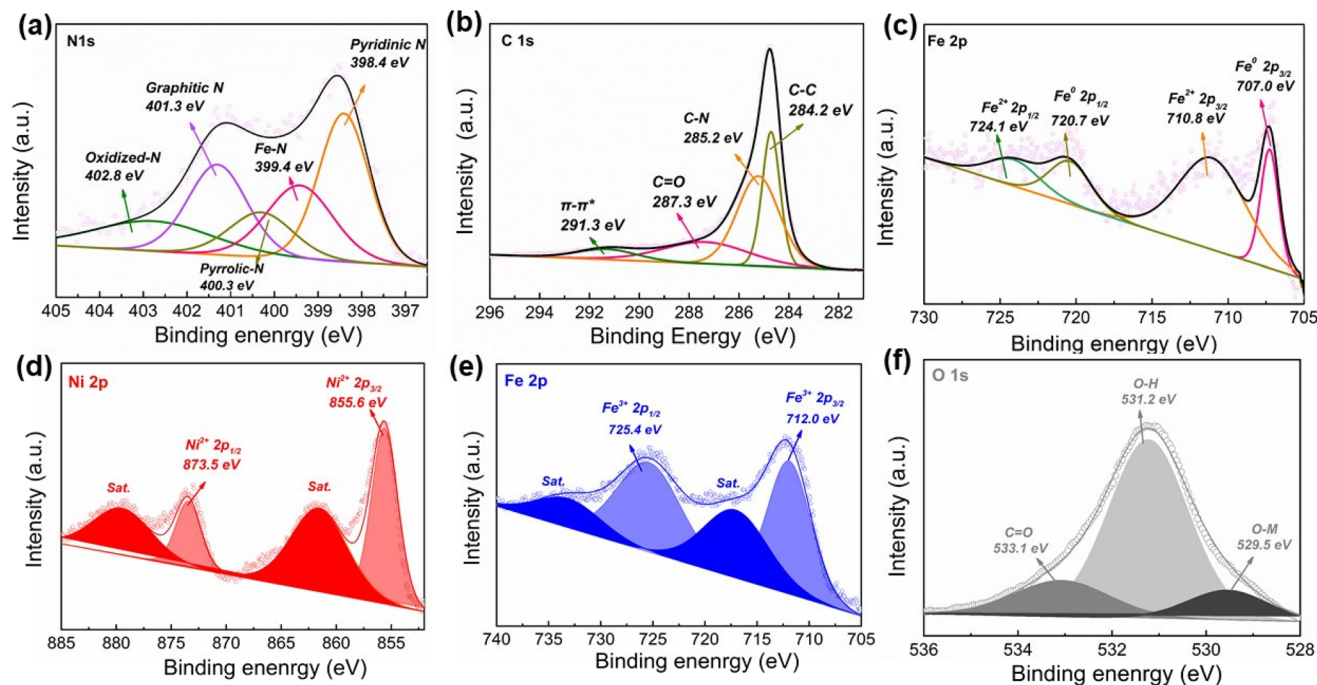**Fig. 2** High-resolution XPS spectra of Fe$_x$NC: (a) N 1s, (b) C 1s and (c) Fe 2p; and Fe$_x$NC@NiFe(OH)$_x$: (d) Ni 2p, (e) Fe 2p and (f) O 1s.

different nitrogen dopants is summarized in Table S2.† The rich nitrogen dopants in Fe$_x$NC have several benefits. Firstly, the pyridinic-N helps to create Lewis basic sites on the carbon surface and edge, which are attractive to O$_2$ molecules.[72] Secondly, the high concentration of the Fe–N$_x$ moiety also contributes to highly efficient sorption and coordination of the intermediate oxygen species during electrocatalysis.[39] Finally, the graphitic-N can donate their electrons to the π-conjugated sp^2 carbon and thus enhance electron mobility.[73,74] The C 2p spectrum of Fe$_x$NC shows four peaks located at 291.3, 287.3, 285.2, and 284.2 eV, which are attributed to π–π*, C=O, C–N and C–C bonds, respectively (Fig. 2b). The result further confirms the formation of N doped carbon moiety on the electrode. High-resolution Fe 2p spectrum is also deconvoluted into zero-valence Fe (707.0 and 720.7 eV) and Fe^{2+}(710.8 and 724.1 eV) (Fig. 2c). Fig. 2d and e demonstrate the high-resolution Ni 2p and Fe 2p spectra of Fe$_x$NC@NiFe(OH)$_x$, and their signals actually reflect the surface chemistry of top layer NiFe(OH)$_x$ (Fig. S6†). In the Fe 2p spectra, the peaks located at 712.0 and 725.4 eV correspond to Fe 2p$_{3/2}$ and Fe 2p$_{1/2}$, respectively, suggesting the dominant oxidation state of the Fe element is trivalent. The deconvoluted peak at 855.6 eV is assigned to Ni 2p$_{3/2}$, while the peak at 873.5 eV is consistent with Ni 2p$_{1/2}$. These two peaks are ascribed to Ni^{2+} in Ni(OH)$_2$. In addition, the O 1s spectrum manifests three characteristic peaks, located at 529.5 (metal–oxygen bond), 531.2 (hydroxyl in oxyhydroxide), and 533.1 eV (adventitious functional group, C=O) (Fig. 2f). Moreover, the stoichiometric composition of Ni to Fe is close to 1 (Table S1 and S3†).

Electrochemical tests are performed in 0.1 M KOH electrolyte using the conventional three-electrode assembly. As shown in Fig. 3a and Table S4,† the Fe$_x$NC@NiFe(OH)$_x$ electrode demonstrates an overpotential of 264 mV at 10 mA cm^{-2} for the OER, which is much lower than that of Fe$_x$NC (377 mV) and noble RuO$_2$ (330 mV). The half-wave potential ($E_{1/2}$) of ORR on Fe$_x$NC@NiFe(OH)$_x$ is as high as 0.858 V (vs. RHE), higher than that of the individual components. It is noted that neither individual Fe$_x$NC nor NiFe(OH)$_x$ shows bifunctional properties towards OER and ORR. A performance indicator, potential difference ΔE ($E_{j=10}$ − E$_{1/2}$), is calculated to further compare the overall oxygen electrocatalytic activity. As shown in Fig. 3b, the composite electrode exhibits the smallest ΔE of 636 mV among all electrodes, especially lower than that of the Pt/C//RuO$_2$ couple. As shown in Fig. S7,† the Tafel slope of the Fe$_x$NC@NiFe(OH)$_x$ electrode is 109 mV dec^{-1}, lower than that of individual Fe$_x$NC (127 mV dec^{-1}), NiFe(OH)$_x$ (151 mV dec^{-1}), and noble Pt (116 mV dec^{-1}), indicating its fast kinetics for ORR. Further dissection of OER reaction kinetics by comparing the Tafel slopes is performed among the different electrodes (Fig. 3c). Fe$_x$NC@NiFe(OH)$_x$ possesses the smallest Tafel slope (60.9 mV Dec^{-1}) than that of NiFe(OH)$_x$ (85.4 mV Dec^{-1}), Fe$_x$NC (84.6 mV Dec^{-1}), and RuO$_2$ (104.6 mV Dec^{-1}). For ORR, we realize that Fe$_x$NC functions as the actual active sites, but the composite electrode also shows a lower onset overpotential and half-wave potential than that of Fe$_x$NC, which arose our attention to analyze the role of outer NiFe(OH)$_x$ clusters. In response, contact angle tests are carried out. As noted in Fig. 3d and Fig. S8,† the surface of the Fe$_x$NC electrode is hydrophobic with a large contact angle of 129°, which would inhibit the access of dissolved oxygen molecules for ORR. In comparison, significant improvement of hydrophilicity is observed on the composite electrode after the incorpor-
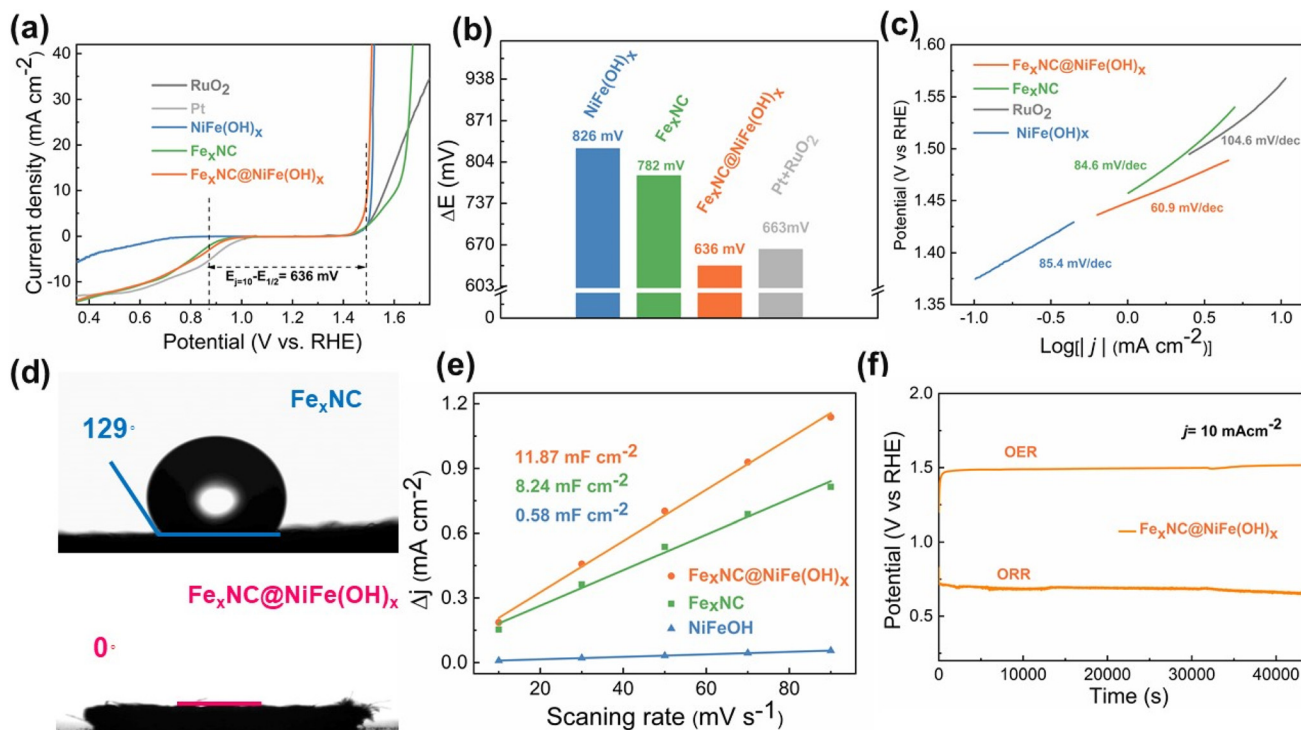
1762 | *Inorg. Chem. Front.*, 2023, **10**, 1758–1768

This journal is © the Partner Organisations 2023

Fig. 3 (a) The polarization curves of different electrodes. (b) Potential difference (ΔE) of NiFe(OH)$_x$, Fe$_x$NC, Fe$_x$NC@NiFe(OH)$_x$, and Pt + RuO$_2$. (c) OER Tafel slopes. (d) Contact angle evaluation on Fe$_x$NC and Fe$_x$NC@NiFe(OH)$_x$. (e) ECSA results of different electrodes. (f) The voltage-time curves of Fe$_x$NC@NiFe(OH)$_x$ at 10 mA cm^{-2}.

ation of the hydrophilic NiFe(OH)$_x$, showing good wetting behaviour. Therefore, the improved wettability of the composite electrode favours the intimate contact between the ORR active sites and oxygen in the electrolyte. Furthermore, the hierarchical pseudo-3D structure constituted by the tubular carbon and NiFe(OH)$_x$ platelets largely increases the electrochemically active surface area (ECSA) to 11.87 mF cm^{-2}, compared with that of the single component (8.24 mF cm^{-2} for Fe$_x$NC and 0.58 mF cm^{-2} for NiFe(OH)$_x$), shown in Fig. 3e and Fig. S9,† thus endowing more accessible active sites for the catalytic reactions. This point can be further confirmed by the BET assessment using nitrogen as the probe gas. As shown in Fig. S10 and Table S5,† among the samples investigated, the composite catalyst electrode possesses a relatively large surface area (5.88 m^2 g^{-1}) and pore volume (0.041 cm^3 g^{-1}), characterized by a range of interconnected porosities from micropores to relatively large mesopores. The results further indicate the intrinsically larger surface area and hierarchical porosities of the composite catalyst, exposing more active sites and facilitating mass transport to enhance electrocatalysis. The long-term durability of the Fe$_x$NC@NiFe(OH)$_x$ electrode towards oxygen electrocatalysis is further evaluated. There is negligible decay for both OER and ORR, suggesting the remarkable stability of the catalyst (Fig. 3f), even superior to the noble metals (Fig. S11†). We also carried out a series of tests to unveil the changes in structure and composition after the electrochemical tests. XRD results indicate no notable phase change

after the reactions except for the emergence of a broad peak at 34.8° on the post-OER electrode, corresponding to Ni$_{1.43}$Fe$_{1.7}$O$_4$ (JCPDS: 80-072) (Fig. S12†).[53] TEM results also reveal a clear crystalline lattice on the edge of the post-OER electrode (Fig. S13a and b†), while the NiFe(OH)$_x$ remains amorphous after long-term ORR (Fig. S13c and d†). Moreover, in the XPS spectra of the post-OER electrode (Fig. S14a–d†), the fitted metal–oxygen peak in O 1s becomes stronger than that of the initial electrode, implying the formation of more metal–oxygen bonds, supporting the emergence of the metal oxide.

There is a trade-off between the catalytic activity and mass transfer capability upon deposition of NiFe(OH)$_x$. As shown in Fig. S15a,† the electrode prepared from the shorter electrode-position time (Fe$_x$NC@NiFe(OH)$_x$-0.3) leads to a large overpotential of 285 mV towards OER at 10 mA cm^{-2} due to the insufficient OER catalytic active sites. While the electrodeposition time becomes long, the electrode (Fe$_x$NC@NiFe(OH)$_x$-10) shows deteriorated ORR performance because its surface is packed with a rather dense NiFe(OH)$_x$ layer, impeding the access of electrolyte to the inner Fe$_x$NC (Fig. S15b†). Hence, a moderate deposition time of 5 min balances the manifold properties, namely, catalytic activity, electrical conductivity, and mass transport, to yield reasonable bifunctional characteristics (Fig. S15c and d†). Therefore, Fe$_x$NC is not densely entrapped inside NiFe(OH)$_x$ in our optimized electrode. On the one hand, the 2D NiFe(OH)$_x$ nanoplates are vertically grown on Fe$_x$NC

This journal is © the Partner Organisations 2023

Inorg. Chem. Front., 2023, **10**, 1758–1768 | **1763**

and thus leave large voids for the electrolyte penetration to active sites for ORR. On the other hand, as the reactants of ORR come from the dissolved oxygen in water, the incorporation of a hydrophilic $NiFe(OH)_x$ layer favors the diffusion of the electrolyte into the active sites.

The excellent oxygen electrocatalytic activity of the composite electrode is further demonstrated in ZAB to showcase practical applications (Fig. S16†). The $Fe_xNC@NiFe(OH)_x$ electrode can be directly used as the air cathode without the need for any binders, simplifying the component structure and ensuring hierarchical pseudo-3D structural integrity. Therefore, the polarization curve of the corresponding ZAB displays a higher discharging voltage and lower charging voltage than other cathode counterparts, implying better energy storage and energy output performance (Fig. 4a). The relatively small voltage gap with the composite electrode agrees well with the above-mentioned bifunctional ability for both OER and ORR (Fig. 4b).

As a result, the cell with the bifunctional electrode can achieve a power density of 85.1 mW cm^{-2}, which is higher than that of Fe_xNC (77.9 mW cm^{-2}), $NiFe(OH)_x$ (70.1 mW cm^{-2}) and is even comparable with that of the $Pt/C//RuO_2$ counterpart (84.9 mW cm^{-2}) (Fig. S17†). The rate capability test further reveals that the ZAB with the composite electrode (ZAB_{CE}) show a higher and more stable discharge plateau at each current density than other counterparts (Fig. 4c). The assembled ZAB shows a stable open circuit voltage of 1.44 V over 50 000 s without severe self-discharge (Fig. 4d). Moreover, the specific capacity of 785.2 mA h g_{Zn}^{-1} is achieved on ZAB_{CE}, which is larger than that of noble metal (721.6 mA h g_{Zn}^{-1}) (Fig. 4e). The battery performance is consistent with the above results, further confirming the merits of our rationally designed composite electrode for bifunctional oxygen electrocatalysis. Finally, the long-time cyclic performance of ZAB is accessed (Fig. 4g). It is evident that ZAB_{CE} shows a very stable lifespan over 350 h (2000 cycles) at the operating current density of 10 mA cm^{-2}, outperforming those with noble metals and single-component electrodes (Fig. S18–S20†), whose cells encounter significant polarization upon cycling. The perform-
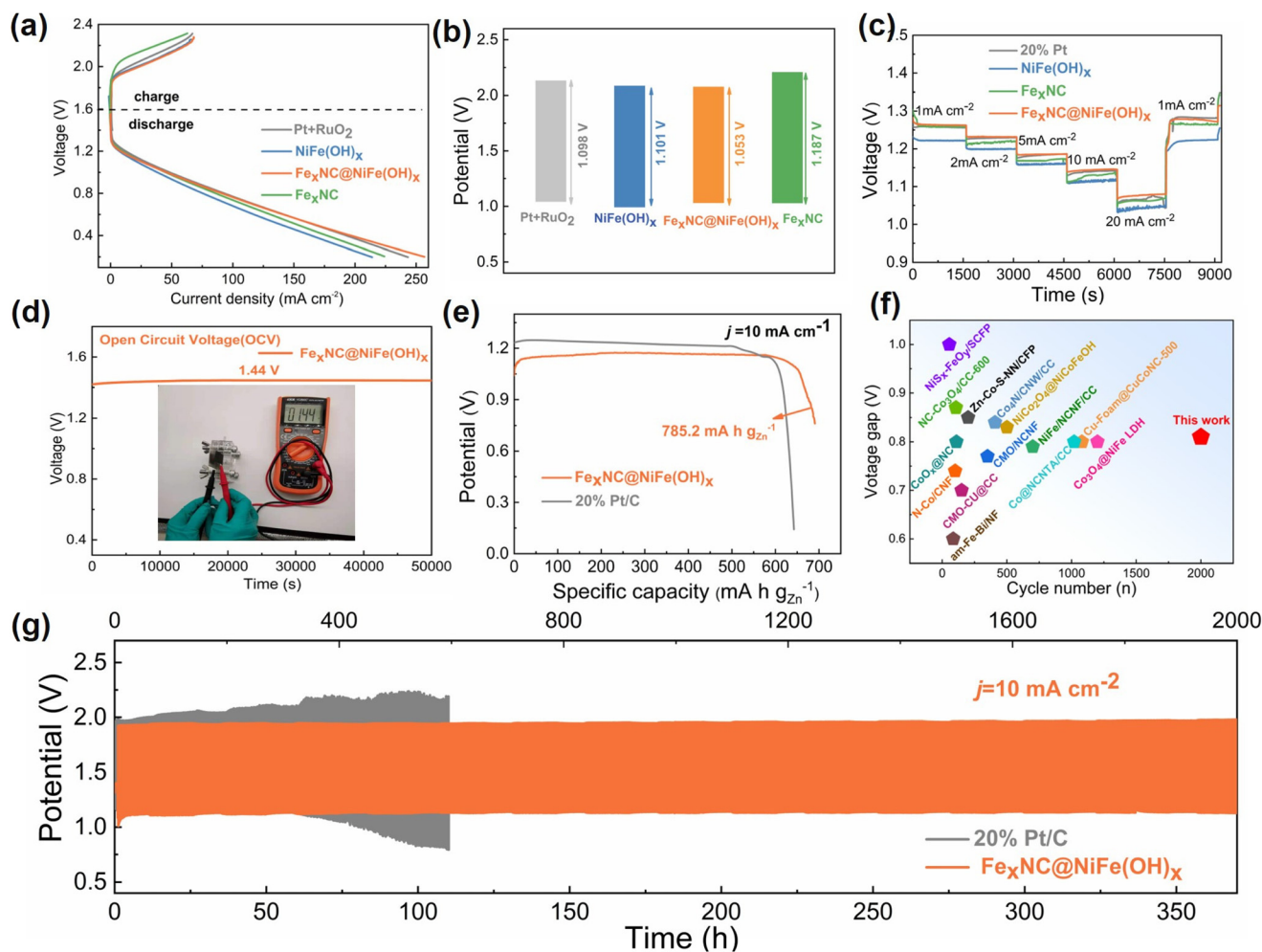

Fig. 4 (a) The charge/discharge polarization curves. (b) Voltage gaps at the current density of 40 mA cm^{-2}. (c) Galvanostatic discharge of Pt/C-ZAB, Fe_xNC-ZAB, $NiFe(OH)_x$-ZAB, and $Fe_xNC@NiFe(OH)_x$-ZAB under different current densities. (d) Open circuit potential, inset: optical image. (e) The specific capacity curves run at 10 mA cm^{-2}. (f) Performance comparison of ZABs using self-supported bifunctional electrodes operating at 10 mA cm^{-2}. (g) The discharge/charge cycle curves of Pt/C-ZAB and $Fe_xNC@NiFe(OH)_x$-ZAB at 10 mA cm^{-2}.

1764 | *Inorg. Chem. Front.*, 2023, **10**, 1758–1768

This journal is © the Partner Organisations 2023

ance also favourably competes with other self-supported electrodes, as outlined in Fig. 4f and Tables S6, S7.† To summarize, our rationally designed hierarchical pseudo-3D composite electrode offers long durability for rechargeable ZABs.

Conclusions

A hierarchical pseudo-3D composite electrode supported on carbon cloth has been successfully fabricated with non-noble metal NiFe(OH)$_x$ clusters grafted over Fe/Fe$_3$C- and N- co-doped carbon nanotubes that are directly grown from carbon-cloth support. The composite electrode rationally integrates the active components for bifunctional properties, achieving an overpotential of 264 mV for OER at a current density of 10 mA cm^{-2} and a half-wave potential of 0.858 V (*vs.* RHE) for ORR. From a series of characterizations, the enhanced performance is due to the following merits: (1) the inner conductive nitrogen-doped carbon nanotubes serve as the pathway for electron transfer, and the appropriate amount of outer NiFe(OH)$_x$ clusters provide interconnected access for electrolyte penetration. (2) The outer layer NiFe(OH)$_x$ tunes the hydrophilicity to cater to the electrode/electrolyte interface. (3) hierarchical pseudo-3D structure endows the composite electrode with an increased electrochemical surface for electrocatalysis. For practical applications, ZAB$_{CE}$ shows a power density of 85.1 mW cm^{-2} and a long cycle life of 350 h (2000 cycles), superior to those using noble metals. This work provides a low-cost alternative to noble metals for oxygen electrocatalysis and offers fresh insights underpinning the rational design of bifunctional oxygen electrodes.

Conflicts of interest

There are no conflicts to declare.

Acknowledgements

References

1 T. Cui, Y. P. Wang, T. Ye, J. Wu, Z. Chen, J. Li, Y. Lei, D. Wang and Y. Li, Engineering dual single-atom sites on 2D ultrathin N-doped carbon nanosheets attaining ultralow-temperature Zinc-air battery, *Angew. Chem., Int. Ed.*, 2022, **61**, e202115219.

2 W. Sun, F. Wang, B. Zhang, M. Zhang, V. Kupers, X. Ji, C. Theile, P. Bieker, K. Xu, C. Wang and M. Winter, A rechargeable Zinc-air battery based on zinc peroxide chemistry, *Science*, 2021, **371**, 46–51.

3 X. Yao, X. Wang, L. Sun, L. Li, E. Kan, B. Ouyang and W. Zhang, Popcorn-like Co$_3$O$_4$ nanoparticles confined in a three-dimensional hierarchical N-doped carbon nanotube network as a highly-efficient trifunctional electrocatalyst for Zinc–air batteries and water splitting devices, *Inorg. Chem. Front.*, 2022, **9**, 2517–2529.

4 H. Dou, M. Xu, Y. Zheng, Z. Li, G. Wen, Z. Zhang, L. Yang, Q. Ma, A. Yu, D. Luo, X. Wang and Z. Chen, Bioinspired tough solid-state electrolyte for flexible ultralong-life Zinc-air battery, *Adv. Mater.*, 2022, **34**, 2110585.

5 Y. Tian, X. Liu, L. Xu, D. Yuan, Y. Dou, J. Qiu, H. Li, J. Ma, Y. Wang, D. Su and S. Zhang, Engineering crystallinity and oxygen vacancies of Co(II) oxide nanosheets for high performance and robust rechargeable Zn–air batteries, *Adv. Funct. Mater.*, 2021, **31**, 2101239.

6 Y. P. Deng, Y. Jiang, R. Liang, S. J. Zhang, D. Luo, Y. Hu, X. Wang, J. T. Li, A. Yu and Z. Chen, Dynamic electrocatalyst with current-driven oxyhydroxide shell for rechargeable Zinc-air battery, *Nat. Commun.*, 2020, **11**, 1952.

7 P. Li, H. Jang, B. Yuan, Z. Wu, X. Liu and J. Cho, Using lithium chloride as a medium to prepare N,P-codoped carbon nanosheets for oxygen reduction and evolution reactions, *Inorg. Chem. Front.*, 2019, **6**, 417–422.

8 Y. Li and J. Lu, Metal–air batteries: Will they be the future electrochemical energy storage device of choice?, *ACS Energy Lett.*, 2017, **2**, 1370–1377.

9 J. S. Lee, T. K. Sun, R. Cao, N.-S. Choi, M. Liu, K. T. Lee and J. Cho, Metal-air batteries with high energy density: Li-air versus Zn-air, *Adv. Energy Mater.*, 2011, **1**, 34–50.

10 C. Cui, X. Ge, T. An, B. Li, D. Wuu, N. N. Tham, K. Zhang, Y. He and Z. Liu, A nanostructured nickel/carbon matrix as an efficient oxygen evolution reaction electrocatalyst for rechargeable Zinc–air batteries, *Inorg. Chem. Front.*, 2019, **6**, 1873–1880.

11 X. Z. Liu, T. Tang, W. J. Jiang, Q. H. Zhang, L. Gu and J. S. Hu, Fe-doped Co$_3$O$_4$ polycrystalline nanosheets as a binder-free bifunctional cathode for robust and efficient Zinc–air batteries, *Chem. Commun.*, 2020, **56**, 5374–5377.

12 Q. Qin, H. Jang, L. Chen, G. Nam, X. Liu and J. Cho, Low loading of Rh$_x$P and RuP on N, P codoped carbon as two trifunctional electrocatalysts for the oxygen and hydrogen electrode reactions, *Adv. Energy Mater.*, 2018, **8**, 1801478.

13 A. K. Worku, D. W. Ayele and N. G. Habtu, Recent advances and future perspectives in engineering of bifunctional electrocatalysts for rechargeable Zinc-air batteries, *Mater. Today Adv.*, 2021, **9**, 100116.

14 Z. F. Huang, J. Wang, Y. Peng, C. Y. Jung, A. Fisher and X. Wang, Design of efficient bifunctional oxygen reduction/evolution electrocatalyst: recent advances and perspectives, *Adv. Energy Mater.*, 2017, **7**, 1700544.

This journal is © the Partner Organisations 2023

Inorg. Chem. Front., 2023, **10**, 1758-1768 | **1765**

15 Y. Zhang, T. Hu, C. Ke, F. Han, W. Xiao and X. Yang, Ru nanoclusters confined on α/β cobalt hydroxide nanosheets as efficient bifunctional oxygen electrocatalysts for Zn–air batteries, *Inorg. Chem. Front.*, 2022, **9**, 5774–5782.

16 H. Su, M. A. Soldatov, V. Roldugin and Q. Liu, Platinum single-atom catalyst with self-adjustable valence state for large-current-density acidic water oxidation, *eScience*, 2022, **2**, 102–109.

17 J. Zhang, Z. Zhao, Z. Xia and L. Dai, A metal-free bifunctional electrocatalyst for oxygen reduction and oxygen evolution reactions, *Nat. Nanotechnol.*, 2015, **10**, 444–452.

18 Y. Chen, S. Ji, S. Zhao, W. Chen, J. Dong, W. C. Cheong, R. Shen, X. Wen, L. Zheng, A. I. Rykov, S. Cai, H. Tang, Z. Zhuang, C. Chen, Q. Peng, D. Wang and Y. Li, Enhanced oxygen reduction with single-atomic-site iron catalysts for a zinc-air battery and hydrogen-air fuel cell, *Nat. Commun.*, 2018, **9**, 5422.

19 W. W. Tian, J. T. Ren and Z. Y. Yuan, *In situ* cobalt-nickel alloy catalyzed nitrogen-doped carbon nanotube arrays as superior freestanding air electrodes for flexible zinc-air and aluminum-air batteries, *Appl. Catal., B*, 2022, **317**, 121764.

20 C. X. Zhao, J. N. Liu, B. Q. Li, D. Ren, X. Chen, J. Yu and Q. Zhang, Multiscale construction of bifunctional electrocatalysts for long-lifespan rechargeable Zinc-air batteries, *Adv. Funct. Mater.*, 2020, **30**, 2003619.

21 A. I. Douka, Y. Xu, H. Yang, S. Zaman, Y. Yan, H. Liu, M. A. Salam and B. Y. Xia, A zeolitic-imidazole frameworks-derived interconnected macroporous carbon matrix for efficient oxygen electrocatalysis in rechargeable Zinc-air batteries, *Adv. Mater.*, 2020, **32**, 2002170.

22 Z. Liang, H. Y. Wang, H. Zheng, W. Zhang and R. Cao, Porphyrin-based frameworks for oxygen electrocatalysis and catalytic reduction of carbon dioxide, *Chem. Soc. Rev.*, 2021, **50**, 2540–2581.

23 J. Tang, Z. Liang, H. Qin, X. Liu, B. Zhai, Z. Su, Q. Liu, H. Lei, K. Liu, C. Zhao, R. Cao and Y. Fang, Large-area free-standing metalloporphyrin-based covalent organic framework films by liquid-air interfacial polymerization for oxygen electrocatalysis, *Angew. Chem. Int. Ed.*, 2023, **62**, e202214449.

24 Z. Y. Mei, S. Cai, G. Zhao, Q. Jing, X. Sheng, J. Jiang and H. Guo, Understanding electronic configurarions and coordination environment for enhanced ORR process and improved Zn-air battery performance, *Energy Storage Mater.*, 2022, **50**, 12–20.

25 Z. Y. Mei, S. Cai, G. Zhao, X. Zou, Y. Fu, J. Jiang, Q. An, M. Li, T. Liu and H. Guo, Boosting the ORR active and Zn-air battery performance through ameliorating the coordination environment of iron phthalocyanine, *Chem. Eng. J.*, 2022, **430**, 132691.

26 Y. J. Li, L. Cui, P. F. Da, K. W. Qiu, W. J. Qin, W. B. Hu, X. W. Du, K. Davey, T. Ling and S. Z. Qiao, Multiscale structural engineering of Ni-Doped CoO nanosheets for Zinc-air batteries with high power density, *Adv. Mater.*, 2018, **30**, 1804653.

27 C. X. Zhao, J. N. Liu, J. Wang, D. Ren, J. Yu, X. Chen, B. Q. Li and Q. Zhang, A DeltaE = 0.63 V bifunctional

oxygen electrocatalyst enables high-rate and long-cycling Zinc-air batteries, *Adv. Mater.*, 2021, **33**, 2008606.

28 J. Qian, X. Guo, T. Wang, P. Liu, H. Zhang and D. Gao, Bifunctional porous Co-doped NiO nanoflowers electrocatalysts for rechargeable zinc-air batteries, *Appl. Catal., B*, 2019, **250**, 71–77.

29 Y. Zhang, Z. Zhang, G. Jiang, A. H. Mamaghani, S. Sy, R. Gao, Y. Jiang, Y. Deng, Z. Bai, L. Yang, A. Yu and Z. Chen, Three-dimensionally ordered mesoporous Co_3O_4 decorated with Mg as bifunctional oxygen electrocatalysts for high-performance zinc-air batteries, *Nano Energy*, 2022, **100**, 107425.

30 Y. Zhao, Q. Sun, X. Liu, D. Li and S. Xing, $Cu/Co/CoS_2$ embedded in S,N-doped carbon as highly efficient oxygen reduction and evolution electrocatalyst for rechargeable zinc–air batteries, *Inorg. Chem. Front.*, 2022, **9**, 2917–2927.

31 H. Lei, Q. Zhang, Z. Liang, H. Guo, Y. Wang, H. Lv, X. Li, W. Zhang, U. P. Apfel and R. Cao, Metal-corrole-based porous organic polymers for electrocatalytic oxygen reduction and evolution reactions, *Angew. Chem., Int. Ed.*, 2022, **61**, e202201104.

32 L. Liu, Y. Wang, F. Yan, C. Zhu, B. Geng, Y. Chen and S. l. Chou, Cobalt-encapsulated nitrogen-doped carbon nanotube arrays for flexible Zinc-air batteries, *Small Methods*, 2019, **4**, 1900571.

33 X. Han, T. Zhang, W. Chen, B. Dong, G. Meng, L. Zheng, C. Yang, X. Sun, Z. Zhuang, D. Wang, A. Han and J. Liu, $Mn-N_4$ oxygen reduction electrocatalyst: operando investigation of active sites and high performance in Zinc-air battery, *Adv. Energy Mater.*, 2020, **11**, 2002753.

34 Z. H. Wang, H. H. Jin, T. Meng, K. Liao, W. Q. Meng, J. L. Yang, D. P. He, Y. L. Xiong and S. C. Mu, Fe, Cu-co-ordinated ZIF-derived carbon framework for efficient oxygen reduction reaction and Zinc-air batteries, *Adv. Funct. Mater.*, 2018, **28**, 1802596.

35 X. Liu, S. Peng, X. Li, C. Liu, J. Zeng, X. Qi and T. Liang, Encapsulation of FeCo–Co nanoparticles in N-Doped carbon nanotubes as bifunctional catalysts for Zn-air battery, *J. Electrochem. Soc.*, 2021, **168**, 090514.

36 P. Rao, D. Wu, T. J. Wang, J. Li, P. Deng, Q. Chen, Y. Shen, Y. Chen and X. Tian, Single atomic cobalt electrocatalyst for efficient oxygen reduction reaction, *eScience*, 2022, **2**, 399–404.

37 L. Zong, X. Chen, S. Liu, K. Fan, S. Dou, J. Xu, X. Zhao, W. Zhang, Y. Zhang, W. Wu, F. Lu, L. Cui, X. Jia, Q. Zhang, Y. Yang, J. Zhao, X. Li, Y. Deng, Y. Chen and L. Wang, Ultrafine Fe/Fe_3C decorated on Fe-N-C as bifunctional oxygen electrocatalysts for efficient Zn-air batteries, *J. Energy Chem.*, 2021, **56**, 72–79.

38 W. Yang, X. Liu, X. Yue, J. Jia and S. Guo, Bamboo-like carbon nanotube/Fe_3C nanoparticle hybrids and their highly efficient catalysis for oxygen reduction, *J. Am. Chem. Soc.*, 2015, **137**, 1436–1439.

39 W. J. Jiang, L. Gu, L. Li, Y. Zhang, X. Zhang, L. J. Zhang, J. Q. Wang, J. S. Hu, Z. Wei and L. J. Wan, Understanding the high activity of Fe-N-C electrocatalysts in oxygen

1766 | *Inorg. Chem. Front.*, 2023, **10**, 1758–1768

This journal is © the Partner Organisations 2023

reduction: Fe/Fe₃C nanoparticles boost the activity of Fe-N(x), *J. Am. Chem. Soc.*, 2016, **138**, 3570–3578.

40 X. Sun, P. Wei, S. Gu, J. Zhang, Z. Jiang, J. Wan, Z. Chen, L. Huang, Y. Xu, C. Fang, Q. Li, J. Han and Y. Huang, Atomic-level Fe-N-C coupled with Fe₃C-Fe Nanocomposites in carbon matrixes as high-efficiency bifunctional oxygen catalysts, *Small*, 2020, **16**, e1906057.

41 W. Weng, J. Zhou, D. Gu and W. Xiao, Thermoelectrochemical formation of Fe/Fe₃C@hollow N-doped carbon in molten salts for enhanced catalysis, *J. Mater. Chem. A*, 2020, **8**, 4800–4806.

42 D. Zhou, P. Li, X. Lin, A. McKinley, Y. Kuang, W. Liu, W. F. Lin, X. Sun and X. Duan, Layered double hydroxide-based electrocatalysts for the oxygen evolution reaction: identification and tailoring of active sites, and superaerophobic nanoarray electrode assembly, *Chem. Soc. Rev.*, 2021, **50**, 8790–8817.

43 M. Gong, Y. Li, H. Wang, Y. Liang, J. Z. Wu, J. Zhou, J. Wang, T. Regier, F. Wei and H. Dai, An advanced Ni–Fe layered double hydroxide electrocatalyst for water oxidation, *J. Am. Chem. Soc.*, 2013, **135**, 8452–8455.

44 A. Sumboja, J. Chen, Y. Zong, P. S. Lee and Z. Liu, NiMn layered double hydroxides as efficient electrocatalysts for the oxygen evolution reaction and their application in rechargeable Zn-air batteries, *Nanoscale*, 2017, **9**, 774–780.

45 Y.-J. Ye, N. Zhang and X.-X. Liu, Amorphous NiFe(oxy) hydroxide nanosheet integrated partially exfoliated graphite foil for high efficiency oxygen evolution reaction, *J. Mater. Chem. A*, 2017, **5**, 24208–24216.

46 M. P. Suryawanshi, U. V. Ghorpade, S. W. Shin, U. P. Suryawanshi, E. Jo and J. H. Kim, Hierarchically coupled Ni:FeOOH nanosheets on 3D N-Doped graphite foam as self-supported electrocatalysts for efficient and durable water oxidation, *ACS Catal.*, 2019, **9**, 5025–5034.

47 M. Kim, D.-H. Nam, H. Y. Park, C. Kwon, K. Eom, S. Yoo, J. Jang, H. J. Kim, E. Cho and H. Kwon, Cobalt-carbon nanofibers as an efficient support-free catalyst for oxygen reduction reaction with a systematic study of active site formation, *J. Mater. Chem. A*, 2015, **3**, 14284–14290.

48 F. Zheng, W. Zhang, X. Zhang, Y. Zhang and W. Chen, Sub-2 nm ultrathin and robust 2D FeNi layered double hydroxide nanosheets packed with 1D FeNi-MOFs for enhanced oxygen evolution electrocatalysis, *Adv. Funct. Mater.*, 2021, **31**, 2103318.

49 D. Li, Z. Han, K. Leng, S. Ma, Y. Wang and J. Bai, Biomass wood-derived efficient Fe–N–C catalysts for oxygen reduction reaction, *J. Mater. Sci.*, 2021, **56**, 12764–12774.

50 Y. Li, M. Gong, Y. Liang, J. Feng, J.-E. Kim, H. Wang, G. Hong, B. Zhang and H. Dai, Advanced Zinc-air batteries based on high-performance hybrid electrocatalysts, *Nat. Commun.*, 2013, **4**, 1805.

51 Q. Wang, L. Shang, R. Shi, X. Zhang, Y. Zhao, G. I. N. Waterhouse, L. Z. Wu, C. H. Tung and T. Zhang, NiFe layered double hydroxide nanoparticles on Co,N-codoped carbon nanoframes as efficient bifunctional cata-

lysts for rechargeable Zinc-air batteries, *Adv. Energy Mater.*, 2017, **7**, 1700467.

52 Q. Wang, H. Miao, S. Sun, Y. Xue and Z. Liu, One-pot synthesis of Co₃O₄/Ag nanoparticles supported on N-doped graphene as efficient bifunctional oxygen catalysts for flexible rechargeable Zinc-air batteries, *Chem. – Eur. J.*, 2018, **24**, 14816–14823.

53 Y. Li, S. Guo, T. Jin, Y. Wang, F. Cheng and L. Jiao, Promoted synergy in core-branch CoP@NiFe–OH nanohybrids for efficient electrochemical-/photovoltage-driven overall water splitting, *Nano Energy*, 2019, **63**, 103821.

54 Y. Li, Z. Dong and L. Jiao, Multifunctional transition metal-based phosphides in energy-related electrocatalysis, *Adv. Energy Mater.*, 2019, **10**, 1902104.

55 W. Wang, Z. Wang, Y. Hu, Y. Liu and S. Chen, A potential-driven switch of activity promotion mode for the oxygen evolution reaction at Co₃O₄/NiOₓHᵧ interface, *eScience*, 2022, **2**, 438–444.

56 J. N. Liu, B. Q. Li, C. X. Zhao, J. Yu and Q. Zhang, A composite bifunctional oxygen electrocatalyst for high-performance rechargeable Zinc-air batteries, *ChemSusChem*, 2020, **13**, 1529–1536.

57 L. Gao, S. Chang and Z. Zhang, High-Quality CoFeP nanocrystal/N, P dual-doped carbon composite as a novel bifunctional electrocatalyst for rechargeable Zn-air battery, *ACS Appl. Mater. Interfaces*, 2021, **13**, 22282–22291.

58 Y. Yan, S. Liang, X. Wang, M. Zhang, S. M. Hao, X. Cui, Z. Li and Z. Lin, Robust wrinkled MoS₂/N-C bifunctional electrocatalysts interfaced with single Fe atoms for wearable Zinc-air batteries, *Proc. Natl. Acad. Sci. U. S. A.*, 2021, **118**, e2110036118.

59 A. Kundu, S. Mallick, S. Ghora and C. R. Raj, Advanced oxygen electrocatalyst for Air-breathing electrode in Zn-air batteries, *ACS Appl. Mater. Interfaces*, 2021, **13**, 40172–40199.

60 Y. Li, H. Li, K. Cao, T. Jin, X. Wang, H. Sun, J. Ning, Y. Wang and L. Jiao, Electrospun three dimensional Co/CoP@nitrogen-doped carbon nanofibers network for efficient hydrogen evolution, *Energy Storage Mater.*, 2018, **12**, 44–53.

61 K. Dong, J. Liang, Y. Wang, Z. Xu, Q. Liu, Y. Luo, T. Li, L. Li, X. Shi, A. M. Asiri, Q. Li, D. Ma and X. Sun, Honeycomb carbon nanofibers: a superhydrophilic O(₂)-entrapping electrocatalyst enables ultrahigh mass activity for the two-electron oxygen reduction reaction, *Angew. Chem., Int. Ed.*, 2021, **60**, 10583–10587.

62 S. Dresp, F. Luo, R. Schmack, S. Kühl, M. Gliech and P. Strasser, An efficient bifunctional two-component catalyst for oxygen reduction and oxygen evolution in reversible fuel cells, electrolyzers and rechargeable air electrodes, *Energy Environ. Sci.*, 2016, **9**, 2020–2024.

63 B. Q. Li, C. X. Zhao, S. Chen, J. N. Liu, X. Chen, L. Song and Q. Zhang, Framework-porphyrin-derived single-atom bifunctional oxygen electrocatalysts and their applications in Zn-air batteries, *Adv. Mater.*, 2019, **31**, 1900592.

This journal is © the Partner Organisations 2023

Inorg. Chem. Front., 2023, **10**, 1758–1768 | **1767**

64 L. Zong, W. Wu, S. Liu, H. Yin, Y. Chen, C. Liu, K. Fan, X. Zhao, X. Chen, F. Wang, Y. Yang, L. Wang and S. Feng, Metal-free, active nitrogen-enriched, efficient bifunctional oxygen electrocatalyst for ultrastable zinc-air batteries, *Energy Storage Mater.*, 2020, **27**, 514–521.

65 X. Bao, K. Xie, Z. Zhang, Z. Liu, H. Zhou, F. Luo, D. Zhou and H.-E. Wang, NiFe-LDHs@MnO$_2$ heterostructure as a bifunctional electrocatalyst for oxygen-involved reactions and Zn-air batteries, *Ionics*, 2022, **28**, 1273–1283.

66 L. Li, P. Nie, Y. Chen and J. Wang, Novel acetic acid induced Na-rich Prussian blue nanocubes with iron defects as cathodes for sodium ion batteries, *J. Mater. Chem. A*, 2019, **7**, 12134–12144.

67 X. Zhang, R. Liu, Y. Zang, G. Liu, S. Liu, G. Wang, Y. Zhang, H. Zhang and H. Zhao, Shrimp-shell derived carbon nano-dots as precursors to fabricate Fe,N-doped porous graphitic carbon electrocatalysts for efficient oxygen reduction in zinc–air batteries, *Inorg. Chem. Front.*, 2016, **3**, 910–918.

68 Y. He, X. Yang, Y. Li, L. Liu, S. Guo, C. Shu, F. Liu, Y. Liu, Q. Tan and G. Wu, Atomically dispersed Fe–Co dual metal sites as bifunctional oxygen electrocatalysts for rechargeable and flexible Zn–air batteries, *ACS Catal.*, 2022, **12**, 1216–1227.

69 W. Cai, R. Chen, H. Yang, H. B. Tao, H. Y. Wang, J. Gao, W. Liu, S. Liu, S. F. Hung and B. Liu, Amorphous versus crystalline in water oxidation catalysis: A case study of NiFe alloy, *Nano Lett.*, 2020, **20**, 4278–4285.

70 J. Liu, J. Zhou, S. Liu, G. Chen, W. Wu, Y. Li, P. Jin and C. Xu, Amorphous NiFe-layered double hydroxides nanosheets for oxygen evolution reaction, *Electrochim. Acta*, 2020, **356**, 136827.

71 H. Gao, W. Sun, X. Tian, J. Liao, C. Ma, Y. Hu, G. Du, J. Yang and C. Ge, Amorphous–amorphous coupling enhancing the oxygen evolution reaction activity and stability of the NiFe-based catalyst, *ACS Appl. Mater. Interfaces*, 2022, **14**, 15205–15213.

72 D. Guo, R. Shibuya, C. Akiba, S. Saji, T. Kondo and J. Nakamura, Active sites of nitrogen-doped carbon materials for oxygen reduction reaction clarified using model catalysts, *Science*, 2016, **351**, 361–365.

73 P. Blonski, J. Tucek, Z. Sofer, V. Mazanek, M. Petr, M. Pumera, M. Otyepka and R. Zboril, Doping with Graphitic Nitrogen Triggers Ferromagnetism in Graphene, *J. Am. Chem. Soc.*, 2017, **139**, 3171–3180.

74 H. B. Yang, J. Miao, S. F. Hung, J. Chen, H. B. Tao, X. Wang, L. Zhang, R. Chen, J. Gao, H. M. Chen, L. Dai and B. Liu, Identification of catalytic sites for oxygen reduction and oxygen evolution in N-doped graphene materials: Development of highly efficient metal-free bifunctional electrocatalyst, *Sci. Adv.*, 2016, **2**, e1501122.